Gastruloid Development Competence Discriminates Different States of Pluripotency

Federica Cermola,[1] Cristina D'Aniello,[1] Rosarita Tatè,[1] Dario De Cesare,[1] Alfonso Martinez-Arias,[2] Gabriella Minchiotti,[1,*] and Eduardo Jorge Patriarca[1,*]

[1]Stem Cell Fate Laboratory, Institute of Genetics and Biophysics "A. Buzzati Traverso", CNR, Naples, Italy
[2]Department of Genetics, University of Cambridge, Cambridge CB2 3EH, UK
*Correspondence: gabriella.minchiotti@igb.cnr.it (G.M.), eduardo.patriarca@igb.cnr.it (E.J.P.)
https://doi.org/10.1016/j.stemcr.2020.12.013

SUMMARY

Floating spheroidal aggregates of mouse embryonic stem cells can develop into polarized/elongated organoids, namely gastruloids. We set up a high-performing assay to measure gastruloid formation efficiency (GFE), and found that GFE decreases as pluripotency progresses from naive (GFE $\geq$ 95%) to primed (GFE = 0) state. Specifically, we show that primed EpiSCs fail to generate proper cell aggregates, while early-primed EpiLCs aggregate but eventually fail to develop into elongated gastruloids. Moreover, we characterized proline-induced cells (PiCs), a LIF-dependent reversible early-primed state of pluripotency, and show that PiCs are able to generate gastruloids (GFE $\sim$ 50%) and are also competent to differentiate into primordial germ cell-like cells. Thus, we propose the GFE assay as a valuable functional tool to discriminate different states of the pluripotency continuum.

INTRODUCTION

Pluripotent stem cells (PSCs) forced to grow under non-adherent culture conditions are inclined to establish cell-cell adhesive interactions and, eventually, generate floating three-dimensional cell aggregates, embryoid bodies (Brickman and Serup, 2017). Under defined culture conditions, small numbers of mouse embryonic stem cells (mESCs) form tightly packed and globular aggregates that develop into organoids that break symmetry and grow in a polarized manner with regard to three orthogonal axes (Baillie-Johnson et al., 2015; Marikawa et al., 2009; Simunovic and Brivanlou, 2017; Turner et al., 2016; Turner et al., 2017; van den Brink et al., 2014; Vianello and Lutolf, 2019). These structures are called "gastruloids" (van den Brink et al., 2014), and the cell's aggregate-to-gastruloid transition has been shown to exhibit some features of mouse embryo gastrulation (Beccari et al., 2018; Turner et al., 2017; van den Brink et al., 2020). Gastruloid development depends on: (1) the mESC line examined; (2) the diameter (150–200 μm) of the initial cell aggregates, which is determined by the number of cells (200–400 cells); and (3) a transient (24 h) treatment of developing aggregates with a WNT (Wingless/Integrated) signaling inducer (Baillie-Johnson et al., 2015; Turner et al., 2017). Depending on the starting conditions, different types of organoids may result from this process, which include not only elongated structures but also atypical structures, large spherical cell masses (proliferation without symmetry breaking), spherical structures with protrusions (multiple elongation attempts), and elongated gastruloid-like aggregates, but with one or a few short ectopic protrusions (Baillie-Johnson et al., 2015; Turner et al., 2017). The reason for these

failures remains largely unknown. It is well known that PSC culture conditions influence the behavior of mESCs and that under standard conditions, e.g., serum and leukemia inhibitory factor (LIF), a culture contains a mixture of different cell populations (Mulas et al., 2019; Munoz Descalzo et al., 2012; Smith, 2017). Growing mESCs in defined media, for instance 2i + LIF, eliminates these heterogeneities and maintains the population in a naive/ground state of pluripotency (Ying et al., 2008). The exit from pluripotency in the presence of fibroblast growth factor (FGF) and ACTIVIN A (F/A) triggers a sequence of mESC transitions through unstable states toward a stable primed pluripotency, represented by EpiSCs, which reflect the post-implantation epiblast (Brons et al., 2007; Morgani et al., 2017; Najm et al., 2011; Tesar et al., 2007). Two examples of transient unstable states are EpiLCs (Murakami et al., 2016) and the formative state (Smith, 2017). Each of the stable states exhibits specific cell organization; whereas naive cells are inclined to establish robust cell-cell adhesive interactions, primed cells are more prone to establishing cell-substrate rather than cell-cell interactions.

Intermediate states of pluripotency can be captured in culture by modulating the level of metabolites in the medium, such as proline and ascorbic acid/vitamin C (D'Aniello et al., 2019b, 2017a; D'Aniello et al., 2017b). Several pieces of evidence indicate that a high proline regimen drives mESCs toward a fully reversible primed pluripotent state (proline-induced cells [PiCs]), which resembles that of EpiLCs (Casalino et al., 2011; Comes et al., 2013; D'Aniello et al., 2019a; Washington et al., 2010). Gastruloids have been shown to mimic aspects of early development and body plan formation and might provide an additional test of the developmental fidelity of
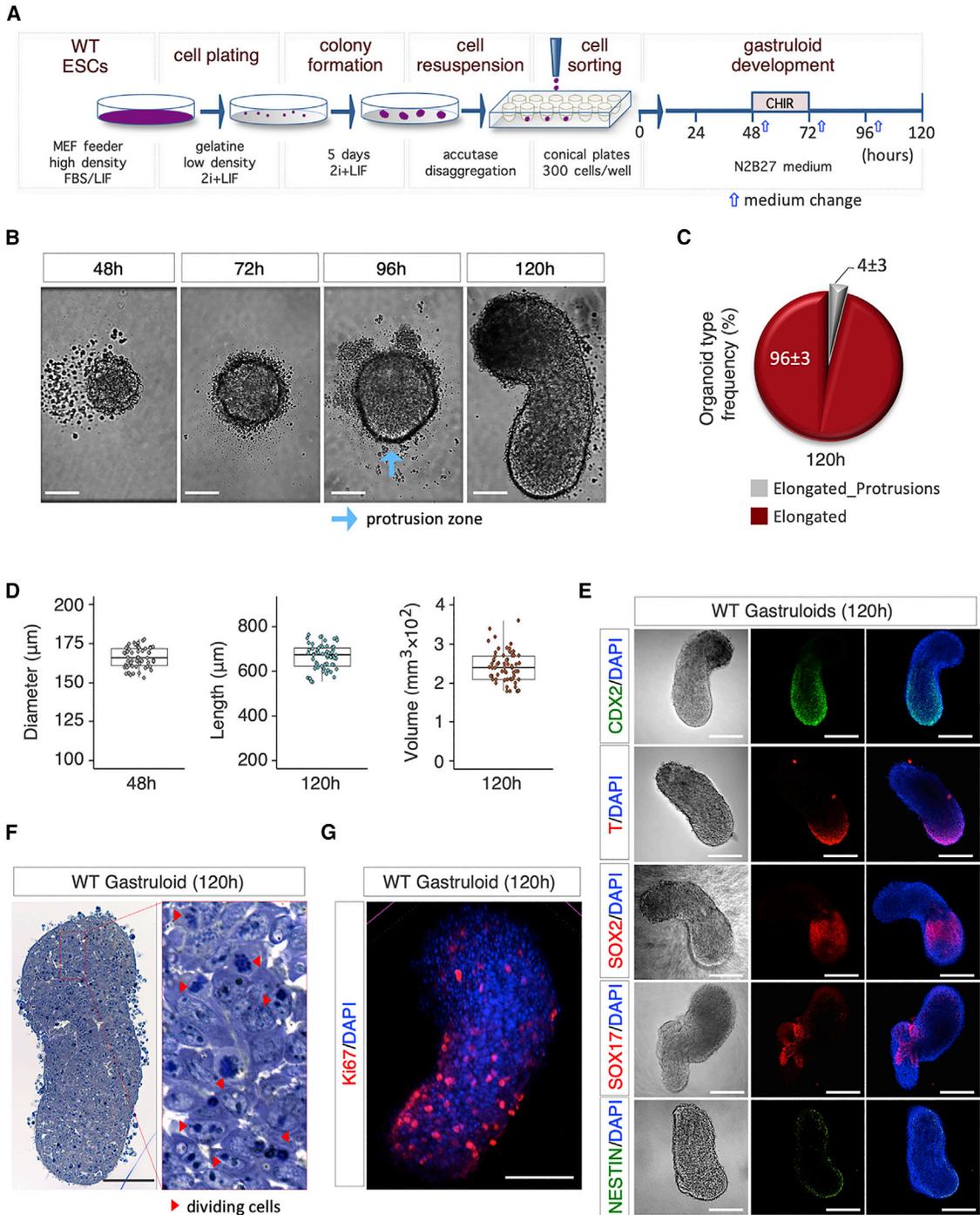
Figure 1. Efficiency of the Optimized Gastruloid Formation Assay

(A) Schematic representation of the experimental design. WT (TBV2) mESCs were plated in 2i + LIF at 250 cells/cm² on gelatin-coated plates.

(B) Representative bright-field images of aggregate-to-gastruloid transition at the indicated time points after aggregation. Light blue arrow indicates the protrusion zone (bar, 100 μm).

(C) Pie chart quantification of the different organoid phenotypes, i.e., without protrusions with a defined A-P axis ("Elongated") or with protrusions and a defined A-P axis ("Elongated_Protrusions"). Data are expressed as mean ± SD (n = 3; 180 gastruloids analyzed).

the cells. Here we report significant technical advances to optimize the gastruloid formation efficiency (hereafter GFE), namely, the fraction of initial cell aggregates that generate fully developed gastruloids, and exploit the potential of GFE as a powerful *in vitro* method to discriminate different states of pluripotency.

RESULTS

Improvement of Gastruloid Formation Efficiency in mESCs

To optimize the efficiency of gastruloid formation, we have adapted the current protocol of Baillie-Johnson et al. (2015), using a TBV2 mESC line (Casalino et al., 2011), particularly by increasing ESC counting accuracy and precision. We first verified the ability of TBV2 mESCs to generate gastruloids using the original protocol (Baillie-Johnson et al., 2015). To this end, FBS/LIF mESCs were seeded at the appropriate density (300 cells/40 μL) in ultra-low attachment plates to force aggregation. Forty-eight hours after aggregation (48 h AA), we observed the formation of spherically shaped cell aggregates with a diameter ranging from 125 to 195 μm (mean = 156 μm) (Figure S1A). Three days later (120 h AA), a major fraction (∼75%) of the primary cell aggregates had become elongated gastruloids (0.5–1 mm long), whereas a significant fraction either remained as unstructured globular cell masses (∼10%) or developed into aberrant organoids (∼15%), displaying one or more ectopic protrusions (Figures S1B and S1C). These results confirmed the occurrence of abnormalities during gastruloid formation, in line with that described with other mESC lines (Baillie-Johnson et al., 2015; Turner et al., 2017). Trying to minimize the fraction of abnormal events and improve GFE, we modified the cell culture conditions (see Figure 1A). First, cells were grown at low density (250 cells/cm^2) on gelatin-coated plates in 2i + LIF, rather than as a confluent (>60%) monolayer. Under these culture conditions, mESCs gave rise to 90%–95% naive/round-domed cell colonies (Figure S1D). Cell dissociation with trypsin reduces the cell-cell adhesion capability of early primed, i.e., L-Pro-induced (Comes et al., 2013), and primed PSCs (Brons et al., 2007), which we reasoned might affect the subsequent aggregation step and eventually reduce the GFE. To overcome this limitation, cells were dissociated with a milder accutase treatment (Figure 1A). Finally, since proper gastruloid development relies on the number of aggregated cells (Baillie-Johnson et al., 2015), we reasoned that the presence of dead cells and/or cellular debris may negatively influence the GFE, increasing the fraction of aberrant embryonic organoids. Thus, to exclude dead cells and cellular debris from the aggregates, living cells were sorted by fluorescence-activated cell sorting (FACS) and a precise/controlled number of cells were seeded and allowed to aggregate (Figures 1A and S1E). The subsequent steps of gastruloid formation assay, including the pulse of CHIR99021 (CHIR; Figure 1A), were carried out as previously described (Baillie-Johnson et al., 2015; Turner et al., 2017; van den Brink et al., 2014). Following this protocol, almost 100% of the developing organoids displayed a single clear protrusion zone at 96 h, thus indicating a well-preserved timing of gastruloid induction (Figure 1B). Later on (120 h), we found a prevalent fraction (95%–98%) of fully developed elongated organoids and a minor fraction (2%–5%) of elongated organoids that, however, displayed one or more short ectopic protrusions (Figure 1C).

To assess the reproducibility of the protocol, we evaluated different parameters, including the diameter of cell aggregates (48 h AA) and both the length and the volume of the developed gastruloids (120 h AA). The diameter of FACS-plated aggregates fluctuated within a significantly lower range (mean = 166 μm; min 153 μm; max 180 μm) compared with that obtained by following the original protocol (mean = 156 μm; min 125 μm; max 195 μm) (Figures 1D and S1A). The expression profile of selected developmental markers, including BRACHYURY (T), SOX2, SOX17, CDX2, and NESTIN, confirmed the establishment of cell lineages and anteroposterior (A-P) axis (Figure 1E). Morphological and immunofluorescence analysis showed that the gastruloids displayed a tightly compacted structure mainly composed of actively dividing cells (Figures 1F and 1G). Interestingly, we observed that excessive narrowing of the forward-scatter light (FSC) and side-scatter light (SSC) values increased the fraction of undeveloped aggregates and strongly reduced the GFE (Figure S1F), suggesting that a certain degree of phenotypic heterogeneity in the stem cell population is essential to generate functional cell aggregates.

We also evaluated the GFE of feeder-free E14 mESCs. ESCs were grown at low density (250 cells/cm^2) on

(D) Boxplot diagrams of aggregate diameter distribution at 48 h (left) and gastruloid length (middle) and volume (π·r^2·h; right) at 120 h (n = 3; 60 gastruloids/time point).

(E) Representative bright-field (left) and confocal images (middle and right) of gastruloids stained with CDX2, NESTIN (green), T/BRA, SOX2, and SOX17 (red). Nuclei were counterstained with DAPI (bar, 200 μm).

(F) Representative pictures of gastruloid sections stained with toluidine blue; red arrows indicate dividing cells (bar, 100 μm).

(G) Representative confocal image of Ki67 immunostaining of gastruloids. Nuclei were counterstained with DAPI (blue) (bar, 100 μm). See also Figure S1.
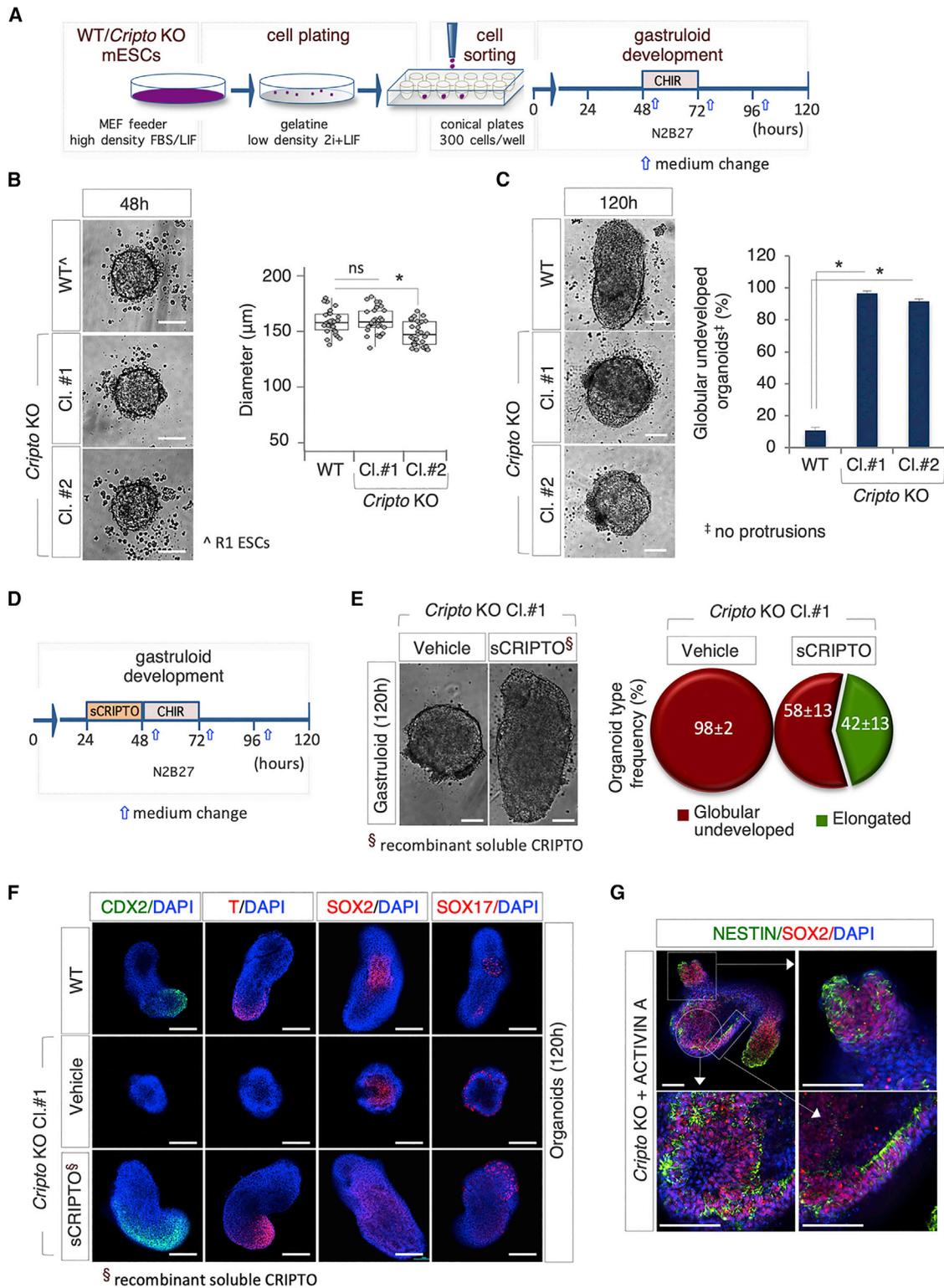
Figure 2. *Cripto* Genetic Ablation Impairs Gastruloid Formation

(A) Schematic representation of the experimental design. WT (R1) and *Cripto* KO mESCs were plated in 2i + LIF at low density on gelatin-coated plates.

(legend continued on next page)

gelatin-coated plates in 2i + LIF, raising up to ~95% of round domed colonies (Figure S1G). Following mild dissociation with accutase, living cells were sorted by FACS (Figure S1H) and subjected to the gastruloid formation protocol as in Figure 1A. In line with that observed with TBV2 ESCs, almost all the aggregates developed elongated gastruloids at 120 h AA (Figure S1I).

Together these findings define the proper culture conditions to increase the GFE of both feeder-free and feeder-dependent mESCs.

Cripto Is Essential for Proper Gastruloid Development

To further validate our experimental approach, we tested the GFE of *Cripto* knockout (KO) mESCs (Parisi et al., 2003). CRIPTO is an obligate co-receptor of the transforming growth factor β (TGF-β) family member NODAL (Minchiotti, 2005) and is required for the proper formation of the A-P axis during embryo development (D'Andrea et al., 2008; Ding et al., 1998). To evaluate the effect of *Cripto* genetic ablation on the GFE, we used two independent *Cripto* KO ESC clones (hereafter Cl.#1 and Cl.#2) (Parisi et al., 2003). Wild-type (WT) and Cl.#1 and Cl.#2 ESCs were seeded at low density on gelatin-coated plates in 2i + LIF; following 5 days in culture, the resulting colonies were dissociated with accutase, and the cells were seeded in 96-well ultra-low plates (300 cells/well) (Figure 2A). At 48 h AA both WT and *Cripto* KO cells generated spherical aggregates with a diameter of ~160 μm (Figure 2B); the aggregates of *Cripto* KO Cl.#2 but not Cl.#1 were slightly smaller compared with control (Figure 2B). At 96 h AA a protrusion zone became evident in the large majority (~90%) of WT and *Cripto* KO aggregates (Figure S2A). Later on, at 120 h AA, a large fraction (~95%) of the WT aggregates became fully elongated organoids (Figure 2C). Conversely, most of the *Cripto* KO aggregates (≥95%) maintained a spheroidal morphology (Figures 2C and S2A), providing evidence that gastruloid development is halted in the absence of *Cripto*. To exclude that the observed phenotype was due to inefficient formation of the cell aggregates, we increased the number of *Cripto* KO cells up to 450 cells/well. Yet,

Cripto KO aggregates maintained a spheroidal morphology and failed to elongate (Figure S2B), thus providing unprecedented evidence that *Cripto* is dispensable for aggregate formation but is essential for gastruloid development. Finally, we performed rescue experiments by using a recombinant soluble active form of CRIPTO (sCRIPTO) (Fiorenzano et al., 2016). *Cripto* KO aggregates were treated with sCRIPTO (from 24 to 48 h AA) or left untreated as control and the GFE was analyzed at 120 h (Figure 2D). A significant fraction (>40%) of sCRIPTO-treated *Cripto* KO aggregates developed elongated gastruloids, which appeared larger in size compared with control (Figure 2E). Immunofluorescence analysis revealed a similar spatial pattern of cells expressing T and CDX2 in fully elongated WT and *Cripto* KO rescued (Cripto KO + sCRIPTO) gastruloids, which, conversely, were almost absent in undeveloped *Cripto* KO organoids (Figure 2F). The expression domain of both genes in the rescued mutants was larger compared with that of WT gastruloids, suggesting that sCRIPTO treatment expanded the posterior mesoderm fate of gastruloids, which might be due to increased NODAL activity (Parisi et al., 2003). Interestingly, *Sox2* and *Sox17* were expressed in the undeveloped *Cripto* KO aggregates (Figures 2F and S2C). Quantitative real-time PCR expression analysis confirmed and extended these findings, e.g., *Brachyury* and *Cdx2* were undetectable in *Cripto* KO organoids, whereas their expression was fully rescued in sCRIPTO-treated *Cripto* KO gastruloids (Figure S2D). Expression of *Sox2* was significantly higher in *Cripto* KO compared with control (Figure S2D); this correlates with the presence of a large area of SOX2-positive cells in the central region of the *Cripto* KO spheroids (Figure 2F) as well as NESTIN-positive cells (Figure S2C). These findings are in line with the fact that *Cripto*-null mutant embryos lack posterior structures (Ding et al., 1998).

To better define the role of NODAL signaling in the inability of *Cripto* KO cells to generate gastruloids, we investigated the effect of ACTIVIN A, which is a potent inducer of NODAL signaling (Pauklin and Vallier, 2015), and found that a transient pulse (24–48 h) of ACTIVIN A (20 ng/mL)

(B) Representative bright-field images (left) and diameter distribution (right) of R1 (WT) and *Cripto* KO clone #1 (Cl.#1) and clone #2 (Cl.#2) mESC-derived aggregates at 48 h (n = 3; 30 gastruloids/condition; *p < 0.01; bar, 100 μm).
(C) Representative bright-field images of WT and *Cripto* KO ESC-derived gastruloids/organoids (left) and quantification (right) of undeveloped WT and *Cripto* KO organoids at 120 h. Data are expressed as mean ± SD (n = 3; 60 organoids/condition; *p < 0.01; bar, 100 μm).
(D) Schematic representation of CRIPTO rescue experiment. Soluble CRIPTO protein (sCRIPTO, 10 μg/mL) was added at 24 h.
(E) Representative bright-field images (left) of *Cripto* KO ± sCRIPTO-derived gastruloids/organoids. Pie chart quantification of the different organoid type frequencies (right). Data are expressed as mean ± SD (n = 3; 30 gastruloids/condition analyzed; bar, 100 μm).
(F) Representative confocal images of WT and *Cripto* KO ± sCRIPTO-derived organoids stained with CDX2 (green), T/BRA, SOX2, and SOX17 (red). Nuclei were counterstained with DAPI (blue) (bar, 100 μm).
(G) Representative confocal images of *Cripto* KO ± ACTIVIN A-derived organoids (120 h AA) with SOX2 (red) and NESTIN (green). Nuclei were counterstained with DAPI (blue) (bar, 100 μm).
See also Figure S2.

in *Cripto* KO aggregates induced the polarization and elongation of a significant fraction (~60%) of mutant aggregates (Figure S2E) that also expressed T at the posterior end of the gastruloid (Figure S2F). However, unlike that observed in WT gastruloids, the expression of CDX2 and SOX17 was undetectable in the ACTIVIN A-induced *Cripto* KO gastruloid-like organoids (Figure S2F), whereas a large area of NESTIN-positive cells was observed (Figures 2G and S2F). These data suggested that ACTIVIN A is able to rescue the polarization and elongation, but fails to induce proper gastruloid development in *Cripto* KO aggregates. Furthermore, a significant fraction of the ACTIVIN A-induced *Cripto* KO organoids displayed ectopic protrusions (Figure S2E). This phenotype could be due, at least in part, to the fact that the ACTIVIN A-treated *Cripto* KO aggregates (48 h AA) were consistently larger in size (>200 μm) compared with those that elongate properly.

The abortive development of *Cripto* KO aggregates validates our experimental approach and provides evidence that *Cripto* is essential for the induction of symmetry breaking (A-P axis formation) in developing gastruloids.

Primed Pluripotency Impairs Gastruloid Development

We then went on and investigated the impact of different pluripotent states from naive to primed on GFE. The naive-to-primed transition was induced as described (Ying et al., 2008). Naive (2i + LIF) ESCs were seeded at low density (1,500 cells/cm^2) on serum-coated plates and grown in N2B27 with F/A for 2 (F/A_2d) and 5 (F/A_5d) days. As expected, expression of the pluripotency markers *Nanog*, *Sox2*, *Rex1*, and *Dppa5a* decreased in F/A_2d compared with 2i + LIF ESCs, while that of the differentiation markers *Cerberus* (*Cer1*), *Brachyury* (*T*), and *Apelin receptor* (*Aplnr*) increased (Figure S3A); the transition from naive to primed was complete in F/A_5d cells. We then assessed the ability of primed cells to revert to the naive state by performing colony formation assays (see Experimental procedures). F/A_2d but not F/A_5d cells were able to generate naive-like dome-shaped colonies (Figures S3B and S3C) and were competent to differentiate into primordial germ-like cells (PGCLCs; see Figure 7), a potential that distinguishes early-primed EpiLCs from primed EpiSCs and naive ESCs (Hayashi et al., 2018). Together these findings are in line with the idea that F/A_2d and F/A_5d cells correspond to early-primed EpiLCs and primed EpiSCs, respectively.

We tested if the GFE could be used to distinguish between naive ESCs (2i + LIF), EpiLCs (F/A_2d), and EpiSCs p0 (F/A_5d) using the optimized gastruloid formation assay (Figure 3A). First, naive and primed cells showed remarkable differences both in the cytometric parameters (Figure S3D) and in the ability to aggregate (Figure 3B). Indeed, while naive cell- and EpiLC-derived aggregates (48 h AA)

were similar in shape (spheroidal) and size (diameter mean ~170 μm) (Figure 3B), EpiSC-derived aggregates were smaller in size (~50 μm) (Figure 3B). Later on, at 120 h AA, while 2i + LIF cell aggregates developed into fully elongated gastruloids (Figures 3C and S3E), the large majority of EpiLC-derived aggregates maintained a spheroidal morphology with a central globular aggregate of cells surrounded by a disorganized and irregular tissue-like structure (Figures 3C and S3E), suggesting that they failed to undergo proper aggregate-to-gastruloid transition. Moreover, EpiSCs-derived aggregates developed into abortive structures whose morphology ranged from spheroidal cell aggregates (~15%) to small irregular cell clusters (~70%; Figure 3C). EpiSCs p0 are highly heterogeneous; however, homogeneous EpiSCs can be stabilized in culture following mechanical passages (Greber et al., 2010). We thus compared the GFE of EpiSCs after six passages in culture (EpiSCs p6) with that of EpiSCs p0 (F/A_5d). Unlike EpiSCs p0, stable EpiSCs were able to aggregate; however, EpiSC p6-derived aggregates displayed heterogeneous morphologies (48 h AA) and failed to properly elongate, maintaining a globular structure with some irregular protrusions (120 h AA; Figure 3D).

We thus assessed whether F/A treatment induced either a sudden loss or a gradual decrease of gastruloid formation competence. To this end, naive ESCs were treated with F/A for different times (12, 24, and 36 h) and their GFE was evaluated. While the GFE of F/A_12 h cells was comparable to that of naive ESCs (~95%), 24 h of F/A treatment completely abolished cells' competence to generate elongated gastruloids (Figure 3E). Indeed, the aggregates derived from F/A-induced cells at both 24 and 36 h failed to elongate, maintaining a spheroidal morphology (Figure 3E).

All together, these findings indicate that, unlike naive ESCs, F/A-induced primed cells are unable to form gastruloids and suggest that F/A treatment causes a sudden loss of ESC gastruloid development competence under these experimental conditions.

F/A-Induced Primed Pluripotency Reduces the Cell Aggregation Propensity

The precise dimensions of mESC aggregates are a critical parameter for gastruloid induction (Baillie-Johnson et al., 2015). Reduced cell aggregate size can be a consequence of either a defective cell aggregation process or a disaggregation subsequent to a normal aggregation process. To investigate this issue directly, we imaged cell aggregate generation at early time points. It has been recently reported that mESCs spontaneously aggregate 8–10 h after seeding (250–300 cells/well) in low-attachment plates (Turner et al., 2017). Accordingly, we observed the presence of irregularly shaped aggregates of naive ESCs already
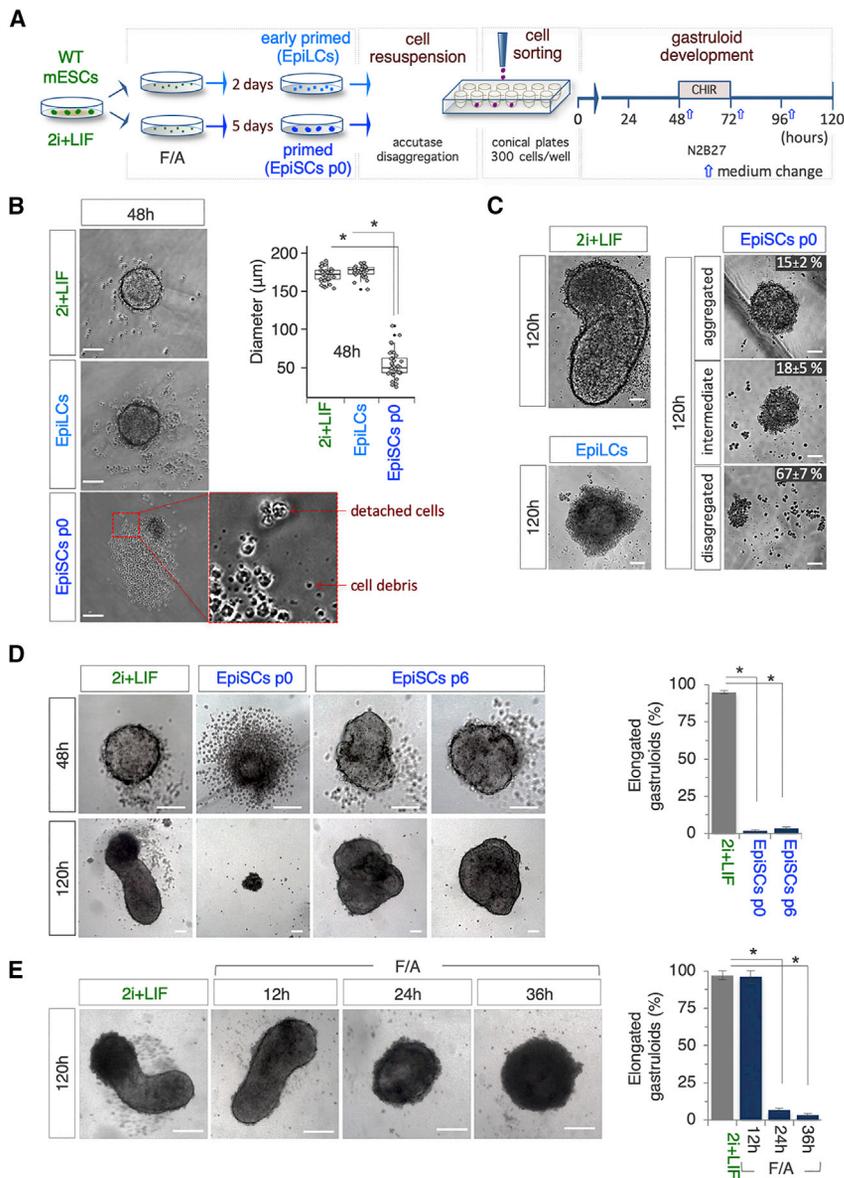
Figure 3. F/A-primed Pluripotent Cells Fail to Generate Gastruloids

(A) Schematic representation of the experimental design. F/A, FGF/ACTIVIN A.

(B) Representative bright-field images of 2i + LIF ESCs, EpiLCs, and EpiSC-derived aggregates at 48 h (left) and boxplot diagram (right) of the distribution of the diameters. Red arrows indicate detached cells and debris (n = 3; 30 gastruloids/condition; bar, 100 μm; *p < 0.01).

(C) Representative bright-field images of the gastruloids and aggregates derived from 2i + LIF ESCs, EpiLCs, and EpiSCs, respectively. Data are expressed as mean ± SD (n = 3; 60 gastruloids/organoids/condition) (bar, 50 μm).

(D) Representative bright-field images (left) of 2i + LIF ESC-, EpiSC p0-, and EpiSC p6-derived aggregates/gastruloid-like organoids at the indicated time points, and quantification (right) of the elongated gastruloids at 120 h. Data are expressed as mean ± SD (n = 3; 60 gastruloids/condition; bar, 100 μm; *p < 0.01).

(E) Representative bright-field images (left) of gastruloids/organoids derived from 2i + LIF- and F/A-treated cells at the indicated time points (bar, 200 μm) and quantification of percentage (right) of elongated gastruloids. Data are expressed as mean ± SD (n = 3; 60 gastruloids/condition; *p < 0.01). See also Figure S3.

at 7 h (mean diameter ∼107 μm) (Figure 4A). Later on (10 h) these naive cell-derived aggregates became highly compacted and displayed a spheroidal morphology (mean diameter ∼100 μm) (Figure 4A). Within this time window, only a few free, non-adherent cells were observed, thus confirming the extraordinary propensity of naive ESCs to generate stable cell-cell interactions. EpiLC-derived early aggregates (7 h) appeared less compacted (mean diameter ∼150 μm) and surrounded by few non-adherent cells (Figure 4A). By 10 h onward, the diameter of the EpiLC aggregates decreased, reaching their minimum (∼135 μm) at around 24 h after seeding (Figure 4A). EpiSC-derived aggregates were much smaller in size (50–70 μm) compared with those generated by EpiLC; further-

more, they were surrounded by a consistent amount of non-adherent cells and cellular debris (Figure 4A). It is thus reasonable to speculate that the generation of gastruloid-developing aggregates requires their compaction/condensation, most likely through the stabilization of cell-cell contacts in the initial cell aggregates. In line with this idea, a gene expression profile analysis (D'Aniello et al., 2017b) showed a significant enrichment in genes related to focal adhesion in EpiSCs p0 compared with 2i + LIF ESCs, which well correlates with a reduced aggregation competence (Figure 4B).

All together these data suggested that F/A-induced primed cells undergo a substantial loss of their capacity to re-establish stable cell-cell contacts following dissociation.

A

→ detached cells

B

Differentially expressed genes
(EpiSCs p0 *vs* 2i+LIF)

5.300 protein coding genes

KEGG Pathway	P-value
Focal adhesion^	1,20E-15
Axon guidance	1,40E-13
MAPK signaling pathway	1,70E-13
WNT signaling pathway	4,40E-09
TGF-beta signaling pathway	1,50E-06

3.300 up-regulated genes

^ also known as cell–matrix adhesions
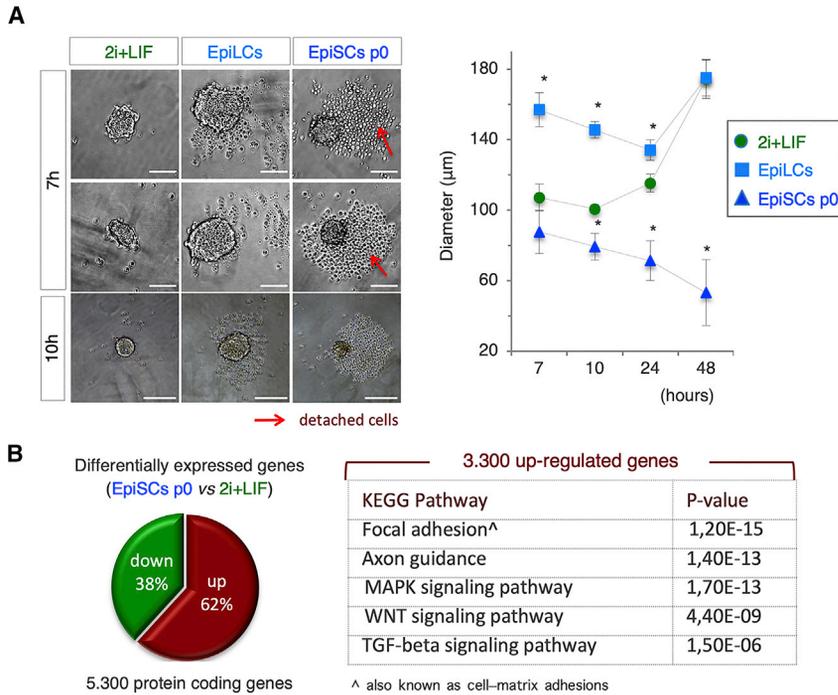
Figure 4. Gastruloid Aggregation Kinetics

(A) Representative bright-field images (left) of aggregates derived from 2i + LIF ESCs, EpiLCs, and EpiSCs p0 at the indicated time points (bar, 100 μm). Red arrows indicate detached cells. Time course quantification (right) of diameters of 2i + LIF ESC-, EpiLC-, and EpiSC p0-derived aggregates. Data are expressed as mean ± SD (n = 3; 30 gastruloids/condition; *p < 0.01).

(B) Pie chart quantification of differentially expressed genes (left) and KEGG pathway enrichment (right) of upregulated genes in EpiSCs p0 versus 2i + LIF.

Gastruloid Development Competence of Proline-Induced Pluripotent Cells

To further evaluate the impact of primed pluripotency on gastruloid development, we assayed the GFE of PiCs. PiCs were obtained by plating mESCs at low clonal density on gelatin-coated plates in FBS/LIF medium supplemented with proline (Comes et al., 2013). As expected, more than 90% of the cell colonies displayed a typical flat and irregular morphology after 4–5 days in culture (Figure S4A). PiCs were dissociated by accutase and subjected to the gastruloid formation protocol (Figure 5A). Control ESCs and PiCs displayed different flow cytometric profiles (FSC and SSC), indicating that a high proline regimen modified ESC size and granularity (Figure S4B). PiC aggregates (48 h AA) were smaller in size (mean diameter = 120 μm) compared with control ESCs (mean diameter = 160 μm) (Figure 5B), and these differences persisted after increasing the number of seeded cells up to 350 (Figure S4C). PiC-derived aggregates started to undergo elongation already at 72 h, whereas, as expected, control ESC aggregates still exhibited a round morphology (Figure 5C). Whereas elongation of PiC-derived aggregates was anticipated by 24–36 h, the overall dimension of the gastruloid-like organoids generated by PiCs was smaller compared with that of ESCs (Figure 5C). These findings suggested that aggregates formed with PiCs elongate earlier compared with aggregates formed with ESCs, a feature that correlates with a propensity to form more compact and thus smaller aggregates. Later on, at 96 h AA, two different morphologies were

observed: the majority of PiC-derived organoids (∼60%) displayed a gastruloid-like fully elongated phenotype, while the remaining (∼40%) maintained the spheroidal morphology of the initial cell aggregates (Figure 5D). The mean length of PiC-derived gastruloids was approximately half that of ESC-derived gastruloids (Figure S4D).

To evaluate if the premature extension and shortened length of PiC-derived gastruloids reflected altered expression of developmental genes, we analyzed the expression pattern of CDX2 and T, and found that they were both expressed in specific territories of PiC elongated organoids (Figure 5E). Frequently, the PiC-derived organoids exhibited a prominent round zone of histological heterogeneity, which stained positive for the mesoendodermal marker SOX17 (Figures 5E and 5F). Large areas of cells expressing the pan-neuronal marker SOX2 were observed adjacent to and surrounding the central region of SOX17-expressing cells (Figure 5G). Histological examination of resin-embedded PiC-derived gastruloids (96 h AA) revealed the presence of both actively dividing and differentiated cells/tissues (Figure 5H). Immunofluorescence analysis of Ki67 confirmed the presence of actively dividing cells (Figure 5I). At 120 h AA, a significant fraction (>50%) of PiC-derived organoids were surrounded by a large number of detached cells (Figures 5J and S4E), suggesting that they underwent early disaggregation.

These findings supported the idea that proline supplementation in the presence of LIF forces cells toward an early and reversible primed state of pluripotency,
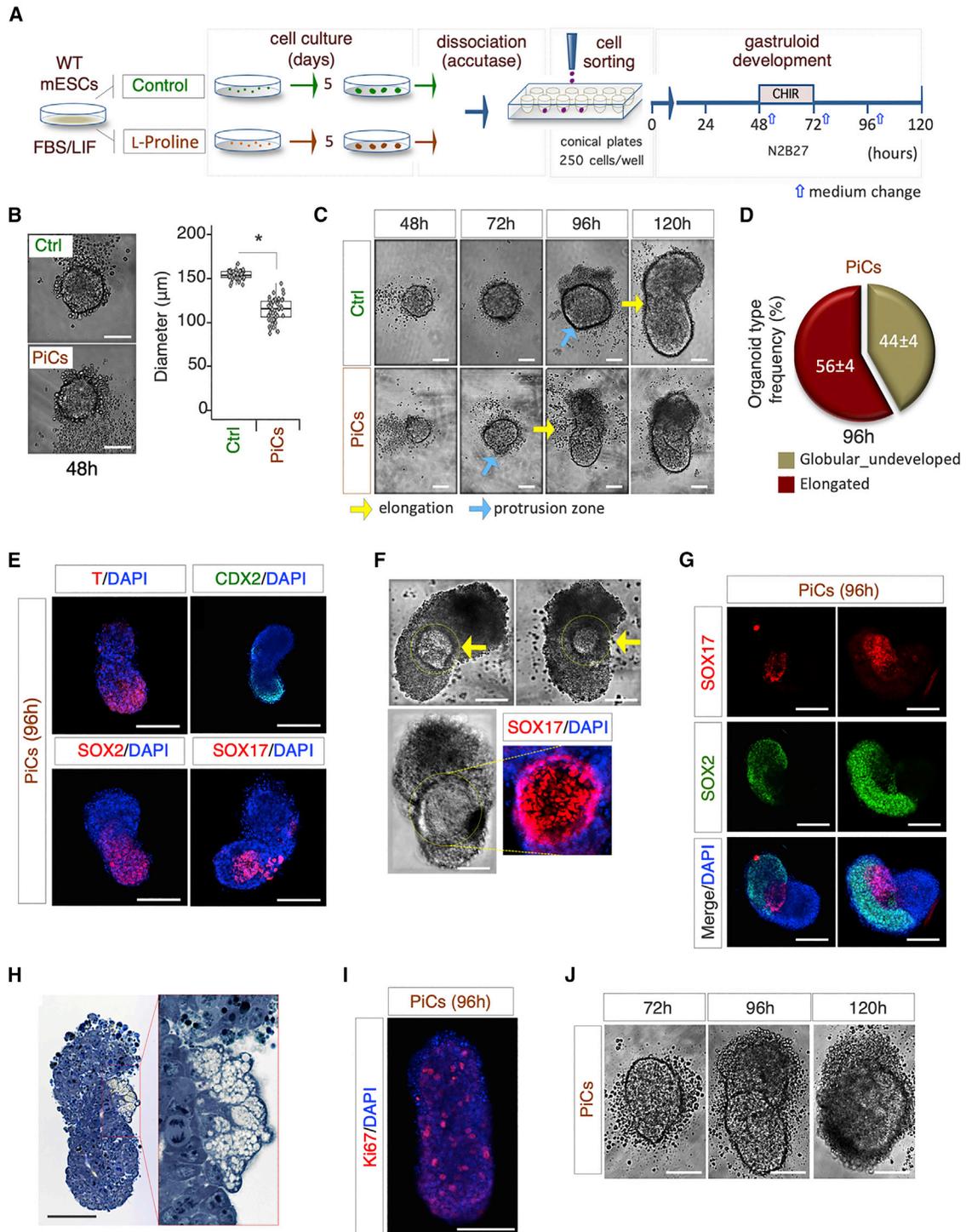
Figure 5. Proline-treated ESCs Are Competent for Gastruloid Formation

(A) Schematic representation of experimental design.

(B) Representative bright-field pictures (left) of control (Ctrl) and PiC-derived aggregates (48 h) and boxplot diagram (right) of diameter distribution (n = 3; 45 gastruloids/condition; *p < 0.01; bar, 100 μm).

(C) Representative bright-field images of globular aggregate-to-elongated gastruloid transition of PiCs and Ctrl cells (bar, 100 μm). Light blue and yellow arrows indicate the protrusion zone and the ovoidal-to-elongated shape transition, respectively.

(legend continued on next page)

which maintains competence to generate gastruloid-like organoids.

LIF Exerts a Dominant Effect on Gastruloid Development Competence of Pluripotent Stem Cells

Several pieces of evidence indicate that EpiLCs and PiCs share features of an early-primed state of pluripotency (D'Aniello et al., 2017b, and data herein); however, we found that PiCs but not EpiLCs generated elongated gastruloids (Figures 3 and 5). Unlike EpiLCs, PiCs strictly rely on LIF (Casalino et al., 2011; D'Aniello et al., 2017a). We thus hypothesized that an active LIF signaling might account, at least in part, for the different GFEs of EpiLCs and PiCs. To address this issue, ESCs were cultured in F/A ± LIF for 48 h, and the GFE of the resulting cells was assessed (Figure 6A). Whereas F/A-induced cells (EpiLCs) failed to generate elongated gastruloids, F/A + LIF-induced cells were able to form gastruloids (GFE ∼ 80%; Figure 6A). Compared with EpiLCs, F/A + LIF-induced cells showed higher expression levels of pluripotency genes including *Tfcp2l1*, *Esrrb*, *Rex1*, *Klf4*, and *Nanog* (Figure 6B) and lower expression of the primed markers *Fgf5* and *Cer1* (Figure 6B) and retained a more homogeneous expression of NANOG (Figure 6C).

Similar results were obtained by adding LIF to EpiLCs in the 0–48 h time window of cell aggregation (Figure 6D), thus suggesting that LIF is able to rescue the gastruloid development competence of EpiLCs.

These data suggested that active LIF signaling exerts a dominant effect over exogenous F/A in providing competence for gastruloid development.

PiCs Are Competent for PGC-like Cell Differentiation

A unique feature of EpiLCs is their ability to differentiate into PGCLCs, whereas both naive cells and EpiSCs are recalcitrant to undergo PGC differentiation (Morgani et al., 2017). We thus investigated if PiCs were competent to generate PGCLC. To this end, ESCs, EpiLCs, and PiCs were dissociated with accutase and seeded (2,500 cells/well) in ultra-low attachment 96-well plates (Figure 7A), and the resulting aggregates were incubated in GK15 medium supplemented with LIF, BMP4, EGF, and SCF as previously described (Hayashi and Saitou, 2013). We first observed that the size of aggregates varied among the different pluripotent states analyzed (Figure 7B). Indeed, PiC aggregates were smaller in size than those of naive ESCs and EpiLCs (Figure 7B). Immunofluorescence analysis of the PGCLC markers BLIMP1 and OCT4 (Hayashi et al., 2018) showed BLIMP1/OCT4 double-positive PGCLCs in both EpiLC- and PiC-derived aggregates (Figure 7C). To corroborate these results, we analyzed the RNA expression profiles of different PGC markers, including *Blimp1*, *Prdm14*, and *Nanos3*, which were all induced in EpiLC- and PiC-derived aggregates (Figure 7D). Finally, immunofluorescence for the PGC marker AP2-γ in a cytospun preparation showed a higher percentage of AP2-γ-positive cells in EpiLC- and PiC-derived compared with naive ESC-derived aggregates (Figure 7E).

All together, these findings indicate that PiCs, like EpiLCs, are competent for PGCLC differentiation, and provide further evidence that a highproline regimen induces an early-primed state of pluripotency, which exhibits a unique competence for both gastruloid formation and differentiation into PGC-like cells.

DISCUSSION

Pluripotency is assessed by combining molecular, phenotypic, and functional analysis. Although the development of global molecular profiling applications, e.g., transcriptomics, epigenomics, metabolomics, and proteomics, has provided comprehensive sets of pluripotency state-associated molecular signatures (Habibi et al., 2013; Pijuan-Sala et al., 2019), the functional assays used to define the different pluripotency state-associated phenotypes, and importantly the developmental fidelity of the cells, require the use of *in vivo* models. Here we propose the GFE assay as

(D) Pie chart quantification of PiC-derived organoid type frequency at 96 h. Data are expressed as mean ± SD (n = 3; 60 gastruloids analyzed).

(E) Representative confocal images of PiC-derived gastruloids stained with T/BRA, SOX2, SOX17 (red), and CDX2 (green). Nuclei were counterstained with DAPI (bar, 200 μm).

(F) Representative bright-field and confocal images of PiC-derived gastruloids (96 h) showing the SOX17-positive area (yellow arrows) (bar, 100 μm).

(G) Representative confocal images of PiC-derived gastruloids stained with SOX17 (red) and SOX2 (green). Nuclei were counterstained with DAPI (bar, 100 μm).

(H) Representative pictures of toluidine blue-stained sections of PiC-derived gastruloids (96 h). Picture enlargement shows a differentiated area (bar, 100 μm).

(I) Representative confocal image of PiC-derived gastruloid stained with Ki67. Nuclei were counterstained with DAPI (bar, 100 μm).

(J) Representative bright-field images of PiC-derived organoids at the indicated time points (bar, 100 μm).

See also Figure S4.
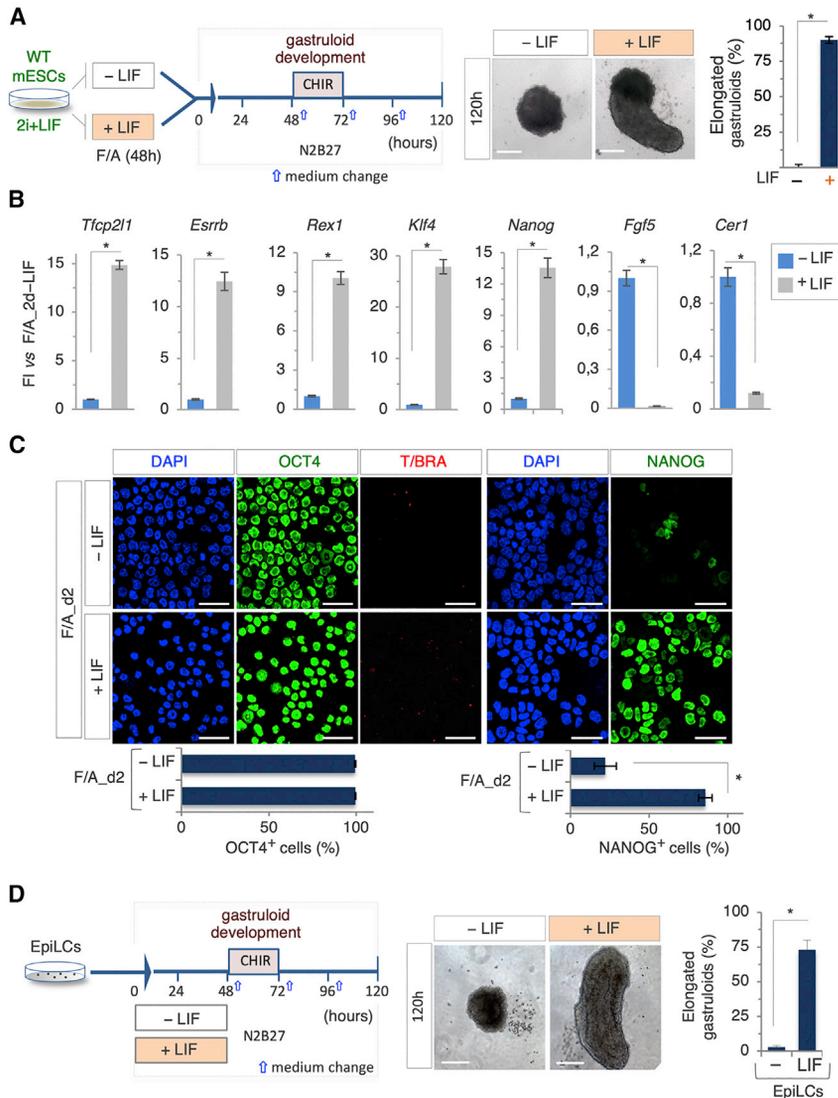
Figure 6. LIF Dominant Effect on Gastruloid Development

(A) Schematic representation of the experimental design (left). ESCs were treated with FGF/ACTIVIN (F/A) ± LIF for 48 h. Representative bright-field images (middle) of F/A_2d ± LIF-derived organoids and quantification (right) of elongated gastruloids (n = 3; 60 gastruloids/condition; *p < 0.01; bar, 100 μm).

(B) Quantitative real-time PCR analysis of pluripotency and differentiation markers in 2d_F/A ± LIF cells. Data represent fold change versus 2d_F/A-LIF; data are normalized to *Gapdh* and are mean ± SD (n = 3; *p < 0.01).

(C) Representative confocal images (top) of OCT4, NANOG (green), and T/BRA (red) staining on cytospun EpiLCs ± LIF. Single-channel images of OCT4 and T/BRA double staining are shown. Nuclei were counterstained with DAPI. Quantification (bottom) of OCT4- and NANOG-positive cells. Data are mean ± SD (bar, 50 μm; n = 3; *p < 0.01).

(D) Schematic representation of the experimental design. EpiLC-derived aggregates were treated ± LIF (0–48 h) (left). Representative bright-field images (middle) of EpiLCs ± LIF-derived organoids, and quantification (right) of elongated gastruloids. Data are expressed as mean ± SD (n = 3; 60 gastruloids/condition; *p < 0.01; bar, 100 μm).

a valuable *in vitro* method to discriminate different states of mouse pluripotency between naive and primed.

We have exploited the potential of the GFE assay to evaluate the developmental potential of different states of pluripotency. We show that, unlike naive ESCs, F/A-induced EpiSCs do not generate elongated gastruloids, and we propose that this is associated with their failure to form proper cellular aggregates following dissociation. In line with these findings, Hayashi and co-workers recently showed that F/A treatment strongly weakens the intrinsic propensity of naive mESCs to aggregate, which eventually leads to failure of differentiation in PGCLCs (Hayashi et al., 2011). This is particularly relevant as re-aggregation of dissociated/singularized cells, i.e., the formation of appropriate cell aggregates, is a critical initial event for proper gastruloid development (Baillie-Johnson et al., 2015;

Turner et al., 2016, 2017) and, more generally, for the generation of different kinds of organoids (Takebe et al., 2012, 2015).

For a functional validation of the assay, we have analyzed the effect of the genetic ablation of the NODAL co-receptor *Cripto* (Minchiotti, 2005) on gastruloid formation. We demonstrate that *Cripto* is essential for symmetry breaking (A-P axis formation) in the developing gastruloids, which is in line with the mutant phenotype of *Cripto* KO embryos that are defective in A-P axis formation (Ding et al., 1998). Interestingly, the addition of either CRIPTO or ACTIVIN A recombinant proteins restores the polarization and elongation of the *Cripto* KO cell aggregates, according to their ability to rescue the zebrafish *oep* (one-eyed pinhead) mutant phenotype (Gritsman et al., 1999). However, while recombinant soluble CRIPTO protein fully
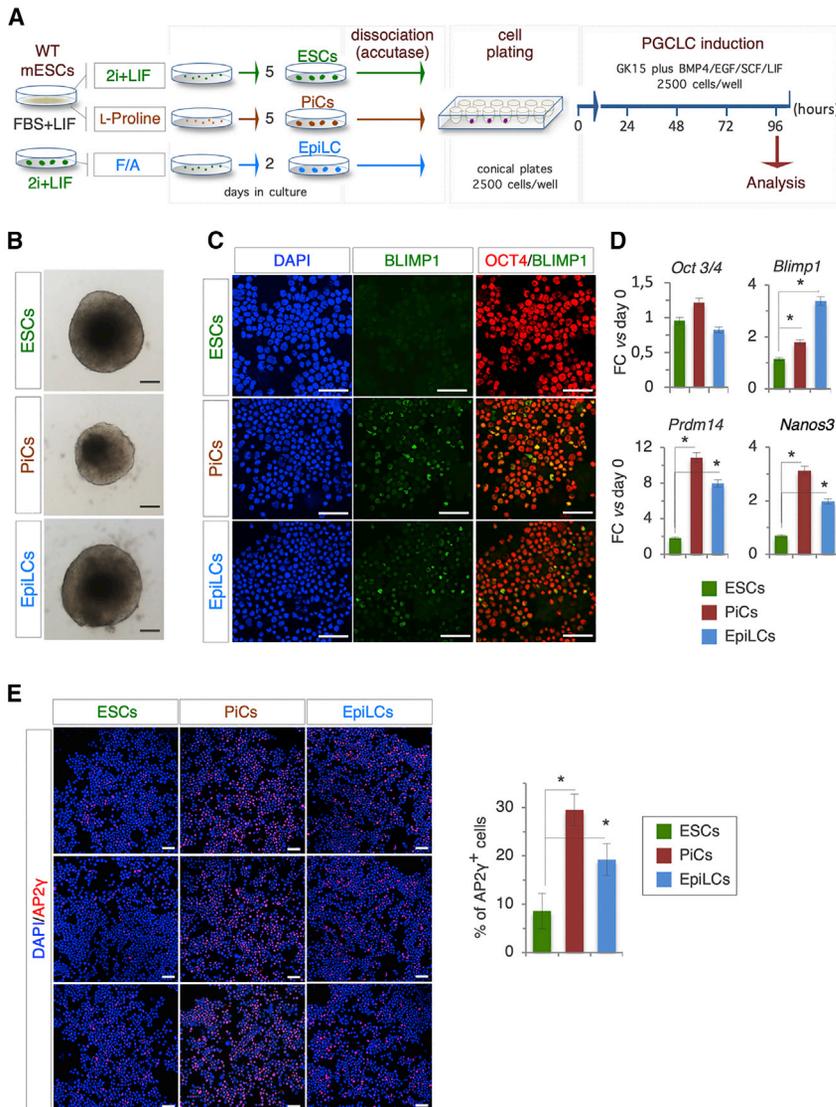
Figure 7. Primordial Germ Cell-like Cell (PGCLC) Competence Discriminates Different Pluripotent States

(A) Schematic representation of the experimental strategy.

(B) Representative bright-field images of 2i + LIF-, PiC-, and EpiLC-derived aggregates (96 h) obtained as described in (A) (bar, 100 μm).

(C) Representative confocal images of cytospun cells from 2i + LIF-, PiC-, and EpiLC-derived aggregates (96 h) double stained with OCT4 (red) and BLIMP1 (green). Nuclei were counterstained with DAPI (bar, 100 μm).

(D) Quantitative real-time PCR analysis of *Oct3/4*, *Blimp1*, *Prdm14*, and *Nanos3* gene expression under the indicated conditions. Data represent fold change versus day 0; data are normalized to *Gapdh* and are mean ± SD (n = 3; *p < 0.01).

(E) Representative confocal images (left) and quantification (right) of AP2-γ-positive cells under indicated conditions (right). Nuclei were counterstained with DAPI. Data are mean ± SD (n = 3; *p < 0.01) (bar, 100 μm).

rescues the morphological and molecular features of *Cripto* KO mutants, ACTIVIN A-treated *Cripto* KO elongated aggregates are still mostly composed of cells expressing neural markers. These results indicate that ACTIVIN A cannot compensate for the lack of *Cripto* in gastruloid formation and suggest that CRIPTO controls gastruloid development through modulation of NODAL signaling (Parisi et al., 2003), which is in line with recent findings that *Nodal* is essential for axial organization and germ-layer specification in gastruloids (Turner et al., 2017), as it is in embryos (Dunn et al., 2004; Turner et al., 2017).

Recent findings reported the generation of gastruloids from human ESCs (Moris et al., 2020). Like EpiSCs, human ESCs rely on FGF and ACTIVIN/NODAL signaling, which may appear to conflict with our results. However, human ESCs are similar to but not the same as EpiSCs, and there

are also differences in the experimental and culture conditions used to generate human versus mouse gastruloids, including pre-treatment of hESCs with CHIR prior to cell aggregation. These features may, at least in part, explain the apparent discrepancy.

Although the molecular mechanism(s) underlying the formation of functional cell aggregates is far from fully elucidated, it is evident that adhesion molecules exert key roles in this process. For instance, F/A-induced primed cells preferentially generate flat rather than domed colonies, thus suggesting that these cells exhibit a higher propensity to generate cell-substrate rather than cell-cell adhesive interactions. In this respect, it has been reported that forced expression of the cell-cell adhesion protein E-CADHERIN improves the chimeric formation ability of EpiSCs (Ohtsuka et al., 2012). Thus, it is reasonable to speculate that

the poor re-aggregation ability of F/A-induced cells is due, at least in part, to reduced expression and/or delocalization of cell-cell adhesion molecules such as E-CADHERIN.

Like EpiSCs, EpiLCs, which represent a transient primed state, fail to generate elongated gastruloids. However, EpiLCs maintain the capacity to aggregate, although the aggregates are less compacted compared with those of naive ESCs. Interestingly, it has been recently reported that compaction is required for the intrinsic induction of TGF-β signaling and chondrogenic differentiation in mesenchymal stem cell aggregates (Sarem et al., 2019). Therefore, it is reasonable to assume that a reduced compaction might generate abortive cell aggregates by preventing the intrinsic activation of key signaling pathways. Indeed, gastruloid development strictly relies on the activation of the WNT and NODAL signaling pathways, whereas high levels of BMP signaling appear dispensable (Turner et al., 2017). Because a WNT signaling agonist is exogenously provided during the GFE assay, we suggest that alteration of NODAL signaling activation could underlie, at least in part, the undeveloped EpiLC phenotype. In line with this idea, both *Nodal* KO (Turner et al., 2017) and *Cripto* KO (data herein) cells generate aggregates displaying similar undeveloped phenotypes.

To further investigate the impact of primed pluripotency on gastruloid formation, we analyzed the GFE of PiCs. PiCs exhibit molecular, metabolic, and functional features of early-primed EpiLCs (Casalino et al., 2011; Comes et al., 2013; D'Aniello et al., 2017b). However, unlike EpiLCs, PiCs form productive, although smaller, aggregates that develop into elongated gastruloids, which properly express the markers of A-P axis formation. We noticed that PiC aggregates start to elongate earlier than controls. The reason PiC-derived aggregates accelerate symmetry breaking is still unknown. Of note, PiC culture contains a minor fraction of late-primed-like cells (D'Aniello et al., 2017b), which might contribute to accelerating gastruloid induction. Interestingly, we also show that PiCs are competent to differentiate into PGCLCs, which is so far considered a feature of EpiLCs.

All together these findings raise the intriguing question of why PiCs but not EpiLCs are competent for gastruloid formation. Like EpiLCs, PiCs strictly depend on activation and maintenance of endogenous bFGF and TGF-β signaling (D'Aniello et al., 2017b); however, unlike EpiLCs, PiCs are also LIF dependent and can be maintained *in vitro* (Casalino et al., 2011). We hypothesize that the gastruloid formation competence of PiCs may rely, at least in part, on the presence of LIF in the culture medium. Indeed, we find that LIF supplementation, either in EpiLC culture medium (F/A + LIF) or in the first 48 h AA window of the gastruloid assay, results in the formation of cell aggregates able to develop into elongated gastruloids. Complementary to these findings, we show that F/A treatment of naive ESCs

induces a sudden loss of gastruloid formation competence. Although the underlying mechanism requires further studies, our findings suggest that LIF exerts a dominant effect over exogenous F/A to provide gastruloid development competence. It would be thus interesting to extend the study to other pluripotent states, as, for instance, the ESC subpopulation that is responsive to both LIF-STAT3 and ACTIVIN-SMAD2/3 (Chang and Li, 2013) and the recently described rosette-stage pluripotency that also relies on LIF (Neagu et al., 2020).

In conclusion, the gastruloid formation assay is a useful and reliable method to evaluate the developmental fidelity of cells. Furthermore, the particular configuration (FACS/ 96 well plates) and efficiency/reproducibility of the GFE assay suggest that it may be suitable for large-scale (high-throughput) phenotype-based genetic and pharmacological screenings for both basic and applied research studies.

EXPERIMENTAL PROCEDURES

ESC Culture Conditions and EpiLC, EpiSC, PiC, and PGCLC Generation

WT TBV2 (129/SvP), E14Tg2a (E14), R1, and *Cripto* KO mouse ESCs (Parisi et al., 2003) were used throughout the study and grown at high density in FBS/LIF as previously described (Fiorenzano et al., 2016). 2i medium (N2B27) was supplemented with PD0325901 (1 μM; Selleckchem), CHIR (3 μM; Selleckchem), and LIF (1,000 u/mL; ESGRO, Millipore). Recombinant sCRIPTO protein was used at 10 μg/mL. All cell lines were routinely tested and confirmed to be free of mycoplasma.

EpiLCs and EpiSCs (p0) were generated from ESCs as described (D'Aniello et al., 2017b). For feeder-free EpiSC passages, EpiSC colonies were mechanically dissociated into small clumps and re-seeded on FBS-coated plates in complete medium as described (Greber et al., 2010). PiCs were generated as previously described (Comes et al., 2013). PGCLC differentiation was performed under floating conditions as previously described (Hayashi and Saitou, 2013). See Supplemental Experimental Procedures for details.

Gastruloid Formation Assay and Analysis

Gastruloid formation assay was performed as described (Baillie-Johnson et al., 2015; van den Brink et al., 2014), with some modifications. Naive and primed PSCs were cultured at low density and the resulting cell colonies were dissociated with accutase (Sigma-Aldrich; 1×, 5 min at 37°C). Cells were thus FACS sorted (FACS ARIAIII, Becton Dickinson) on the basis of FSC-A and SSC-A parameters, excluding cellular debris and dead cells, and seeded in N2B27 at 2.5–4.5 × 10^2 cells/well (40 μL) in U-shaped ultra-low attachment 96 multiwell plates (Corning Costar) and allowed to aggregate. At 48 h AA, CHIR was added (3 μM) to the culture medium and maintained for 24 h. From 72 h onward, the medium (150 μL) was refreshed daily up to 120 h. For treatment at 24 h AA, 20 μL of medium was carefully removed with a multichannel pipette and replaced with an equal amount of N2B27 supplemented with either sCRIPTO or ACTIVIN A at the indicated

concentration. Gastruloids were collected randomly at different time points and imaged using either an Evos cell imaging system or Levenhuk M500 base digital camera for microscopes imaging system.

Immunofluorescence staining on gastruloids was performed as previously described (Baillie-Johnson et al., 2015). Primary and secondary antibodies are listed in Table S2.

For histological analysis, gastruloids were fixed in 2% glutaraldehyde/4% paraformaldehyde, post-fixed in osmium tetraoxide, dehydrated, and embedded in Epon 812 (Polyscience, Niles, IL, USA). Five-micrometer sections were cut using a Leica Ultracut UCT ultramicrotome (Leica Microsystems) and stained with toluidine blue (1% in water, 10 min at room temperature). Images were obtained with an ECLIPSE Ni-E microscope.

RNA Extraction and Quantitative Real-Time PCR

Total RNAs were isolated using either the RNeasy kit or Trizol (Invitrogen) and reverse transcribed using a QuantiTect reverse transcription kit (Qiagen). Quantitative real-time PCR was performed using the SYBR green PCR master mix (FluoCycle II SYBR, EuroClone). Primers are listed in Table S1.

Statistical Analysis

The number of independent experiments is reported as "n" in the caption of each figure and the total sample size is indicated.

Statistical significance was determined by a two-tailed paired Student's t test. p values of ≤ 0.01 were considered statistically significant. Results are presented as the mean ± SD or as a boxplot/dot plot displaying minimum, first quartile, median, third quartile, and maximum. Boxplot/dot plots were generated using RStudio software (https://www.rstudio.com/).

SUPPLEMENTAL INFORMATION

Supplemental Information can be found online at https://doi.org/10.1016/j.stemcr.2020.12.013.

AUTHOR CONTRIBUTIONS

F.C., A.M-A., G.M., and E.J.P. conceived and designed the study. F.C., C.D'A., R.T., D.D.C., and E.J.P. performed the experiments. F.C. performed statistical analysis. C.D'A., A.M-A., D.D.C., and G.M. gave conceptual advice and contributed to the editing of the manuscript. F.C. and E.J.P. wrote the manuscript.

REFERENCES

Baillie-Johnson, P., van den Brink, S.C., Balayo, T., Turner, D.A., and Martinez Arias, A. (2015). Generation of aggregates of mouse embryonic stem cells that show symmetry breaking, polarization and emergent collective behaviour in vitro. J. Vis. Exp., 53252.

Beccari, L., Moris, N., Girgin, M., Turner, D.A., Baillie-Johnson, P., Cossy, A.C., Lutolf, M.P., Duboule, D., and Arias, A.M. (2018). Multi-axial self-organization properties of mouse embryonic stem cells into gastruloids. Nature 562, 272–276.

Brickman, J.M., and Serup, P. (2017). Properties of embryoid bodies. Wiley Interdiscip. Rev. Dev. Biol. 6. https://doi.org/10.1002/wdev.259.

Brons, I.G., Smithers, L.E., Trotter, M.W., Rugg-Gunn, P., Sun, B., Chuva de Sousa Lopes, S.M., Howlett, S.K., Clarkson, A., Ahrlund-Richter, L., Pedersen, R.A., et al. (2007). Derivation of pluripotent epiblast stem cells from mammalian embryos. Nature 448, 191–195.

Casalino, L., Comes, S., Lambazzi, G., De Stefano, B., Filosa, S., De Falco, S., De Cesare, D., Minchiotti, G., and Patriarca, E.J. (2011). Control of embryonic stem cell metastability by L-proline catabolism. J. Mol. Cell Biol. 3, 108–122.

Chang, K.H., and Li, M. (2013). Clonal isolation of an intermediate pluripotent stem cell state. Stem Cells 31, 918–927.

Comes, S., Gagliardi, M., Laprano, N., Fico, A., Cimmino, A., Palamidessi, A., De Cesare, D., De Falco, S., Angelini, C., Scita, G., et al. (2013). L-Proline induces a mesenchymal-like invasive program in embryonic stem cells by remodeling H3K9 and H3K36 methylation. Stem Cell Rep. 1, 307–321.

D'Andrea, D., Liguori, G.L., Le Good, J.A., Lonardo, E., Andersson, O., Constam, D.B., Persico, M.G., and Minchiotti, G. (2008). Cripto promotes A-P axis specification independently of its stimulatory effect on Nodal autoinduction. J. Cell Biol. 180, 597–605.

D'Aniello, C., Cermola, F., Palamidessi, A., Wanderlingh, L.G., Gagliardi, M., Migliaccio, A., Varrone, F., Casalino, L., Matarazzo, M.R., De Cesare, D., et al. (2019a). Collagen prolyl hydroxylation-dependent metabolic perturbation governs epigenetic remodeling and mesenchymal transition in pluripotent and cancer cells. Cancer Res. 79, 3235–3250.

D'Aniello, C., Cermola, F., Patriarca, E.J., and Minchiotti, G. (2017a). Vitamin C in stem cell biology: impact on extracellular matrix homeostasis and epigenetics. Stem Cells Int. 2017, 8936156.

D'Aniello, C., Cermola, F., Patriarca, E.J., and Minchiotti, G. (2019b). Metabolic-Epigenetic Axis in pluripotent state transitions. Epigenomes 3, 13.

D'Aniello, C., Habibi, E., Cermola, F., Paris, D., Russo, F., Fiorenzano, A., Di Napoli, G., Melck, D.J., Cobellis, G., Angelini, C., et al. (2017b). Vitamin C and l-proline antagonistic effects capture

alternative states in the pluripotency continuum. Stem Cell Rep. *8*, 1–10.

Ding, J., Yang, L., Yan, Y.T., Chen, A., Desai, N., Wynshaw-Boris, A., and Shen, M.M. (1998). Cripto is required for correct orientation of the anterior-posterior axis in the mouse embryo. Nature *395*, 702–707.

Dunn, N.R., Vincent, S.D., Oxburgh, L., Robertson, E.J., and Bikoff, E.K. (2004). Combinatorial activities of Smad2 and Smad3 regulate mesoderm formation and patterning in the mouse embryo. Development *131*, 1717–1728.

Fiorenzano, A., Pascale, E., D'Aniello, C., Acampora, D., Bassalert, C., Russo, F., Andolfi, G., Biffoni, M., Francescangeli, F., Zeuner, A., et al. (2016). Cripto is essential to capture mouse epiblast stem cell and human embryonic stem cell pluripotency. Nat. Commun. *7*, 12589.

Greber, B., Wu, G., Bernemann, C., Joo, J.Y., Han, D.W., Ko, K., Tapia, N., Sabour, D., Sterneckert, J., Tesar, P., et al. (2010). Conserved and divergent roles of FGF signaling in mouse epiblast stem cells and human embryonic stem cells. Cell Stem Cell *6*, 215–226.

Gritsman, K., Zhang, J., Cheng, S., Heckscher, E., Talbot, W.S., and Schier, A.F. (1999). The EGF-CFC protein one-eyed pinhead is essential for nodal signaling. Cell *97*, 121–132.

Habibi, E., Brinkman, A.B., Arand, J., Kroeze, L.I., Kerstens, H.H., Matarese, F., Lepikhov, K., Gut, M., Brun-Heath, I., Hubner, N.C., et al. (2013). Whole-genome bisulfite sequencing of two distinct interconvertible DNA methylomes of mouse embryonic stem cells. Cell Stem Cell *13*, 360–369.

Hayashi, K., Ohta, H., Kurimoto, K., Aramaki, S., and Saitou, M. (2011). Reconstitution of the mouse germ cell specification pathway in culture by pluripotent stem cells. Cell *146*, 519–532.

Hayashi, K., and Saitou, M. (2013). Generation of eggs from mouse embryonic stem cells and induced pluripotent stem cells. Nat. Protoc. *8*, 1513–1524.

Hayashi, M., Kawaguchi, T., Durcova-Hills, G., and Imai, H. (2018). Generation of germ cells from pluripotent stem cells in mammals. Reprod. Med. Biol. *17*, 107–114.

Marikawa, Y., Tamashiro, D.A., Fujita, T.C., and Alarcon, V.B. (2009). Aggregated P19 mouse embryonal carcinoma cells as a simple in vitro model to study the molecular regulations of mesoderm formation and axial elongation morphogenesis. Genesis *47*, 93–106.

Minchiotti, G. (2005). Nodal-dependant Cripto signaling in ES cells: from stem cells to tumor biology. Oncogene *24*, 5668–5675.

Morgani, S., Nichols, J., and Hadjantonakis, A.K. (2017). The many faces of Pluripotency: in vitro adaptations of a continuum of in vivo states. BMC Dev. Biol. *17*, 7.

Moris, N., Anlas, K., van den Brink, S.C., Alemany, A., Schroder, J., Ghimire, S., Balayo, T., van Oudenaarden, A., and Martinez Arias, A. (2020). An in vitro model of early anteroposterior organization during human development. Nature *582*, 410–415.

Mulas, C., Kalkan, T., von Meyenn, F., Leitch, H.G., Nichols, J., and Smith, A. (2019). Defined conditions for propagation and manipulation of mouse embryonic stem cells. Development *146*, dev173146.

Munoz Descalzo, S., Rue, P., Garcia-Ojalvo, J., and Martinez Arias, A. (2012). Correlations between the levels of Oct4 and Nanog as a signature for naive pluripotency in mouse embryonic stem cells. Stem Cells *30*, 2683–2691.

Murakami, K., Gunesdogan, U., Zylicz, J.J., Tang, W.W.C., Sengupta, R., Kobayashi, T., Kim, S., Butler, R., Dietmann, S., and Surani, M.A. (2016). NANOG alone induces germ cells in primed epiblast in vitro by activation of enhancers. Nature *529*, 403–407.

Najm, F.J., Chenoweth, J.G., Anderson, P.D., Nadeau, J.H., Redline, R.W., McKay, R.D., and Tesar, P.J. (2011). Isolation of epiblast stem cells from preimplantation mouse embryos. Cell Stem Cell *8*, 318–325.

Neagu, A., van Genderen, E., Escudero, I., Verwegen, L., Kurek, D., Lehmann, J., Stel, J., Dirks, R.A.M., van Mierlo, G., Maas, A., et al. (2020). In vitro capture and characterization of embryonic rosette-stage pluripotency between naive and primed states. Nat. Cell Bio.l *22*, 534–545.

Ohtsuka, S., Nishikawa-Torikai, S., and Niwa, H. (2012). E-cadherin promotes incorporation of mouse epiblast stem cells into normal development. PLoS One *7*, e45220.

Parisi, S., D'Andrea, D., Lago, C.T., Adamson, E.D., Persico, M.G., and Minchiotti, G. (2003). Nodal-dependent Cripto signaling promotes cardiomyogenesis and redirects the neural fate of embryonic stem cells. J. Cell Biol. *163*, 303–314.

Pauklin, S., and Vallier, L. (2015). Activin/Nodal signalling in stem cells. Development *142*, 607–619.

Pijuan-Sala, B., Griffiths, J.A., Guibentif, C., Hiscock, T.W., Jawaid, W., Calero-Nieto, F.J., Mulas, C., Ibarra-Soria, X., Tyser, R.C.V., Ho, D.L.L., et al. (2019). A single-cell molecular map of mouse gastrulation and early organogenesis. Nature *566*, 490–495.

Sarem, M., Otto, O., Tanaka, S., and Shastri, V.P. (2019). Cell number in mesenchymal stem cell aggregates dictates cell stiffness and chondrogenesis. Stem Cell Res. Ther. *10*, 10.

Simunovic, M., and Brivanlou, A.H. (2017). Embryoids, organoids and gastruloids: new approaches to understanding embryogenesis. Development *144*, 976–985.

Smith, A. (2017). Formative pluripotency: the executive phase in a developmental continuum. Development *144*, 365–373.

Takebe, T., Enomura, M., Yoshizawa, E., Kimura, M., Koike, H., Ueno, Y., Matsuzaki, T., Yamazaki, T., Toyohara, T., Osafune, K., et al. (2015). Vascularized and complex organ buds from diverse tissues via mesenchymal cell-driven condensation. Cell Stem Cell *16*, 556–565.

Takebe, T., Sekine, K., Suzuki, Y., Enomura, M., Tanaka, S., Ueno, Y., Zheng, Y.W., and Taniguchi, H. (2012). Self-organization of human hepatic organoid by recapitulating organogenesis in vitro. Transpl. Proc. *44*, 1018–1020.

Tesar, P.J., Chenoweth, J.G., Brook, F.A., Davies, T.J., Evans, E.P., Mack, D.L., Gardner, R.L., and McKay, R.D. (2007). New cell lines from mouse epiblast share defining features with human embryonic stem cells. Nature *448*, 196–199.

Turner, D.A., Baillie-Johnson, P., and Martinez Arias, A. (2016). Organoids and the genetically encoded self-assembly of embryonic stem cells. Bioessays *38*, 181–191.

Turner, D.A., Girgin, M., Alonso-Crisostomo, L., Trivedi, V., Baillie-Johnson, P., Glodowski, C.R., Hayward, P.C., Collignon, J., Gustavsen, C., Serup, P., et al. (2017). Anteroposterior polarity and elongation in the absence of extra-embryonic tissues and of spatially localised signalling in gastruloids: mammalian embryonic organoids. Development 144, 3894–3906.

van den Brink, S.C., Alemany, A., van Batenburg, V., Moris, N., Blotenburg, M., Vivie, J., Baillie-Johnson, P., Nichols, J., Sonnen, K.F., Martinez Arias, A., et al. (2020). Publisher Correction: single-cell and spatial transcriptomics reveal somitogenesis in gastruloids. Nature 579, E11.

van den Brink, S.C., Baillie-Johnson, P., Balayo, T., Hadjantonakis, A.K., Nowotschin, S., Turner, D.A., and Martinez Arias, A. (2014). Symmetry breaking, germ layer specification and axial organisation in aggregates of mouse embryonic stem cells. Development 141, 4231–4242.

Vianello, S., and Lutolf, M.P. (2019). Understanding the mechanobiology of early mammalian development through bioengineered models. Dev. Cell 48, 751–763.

Washington, J.M., Rathjen, J., Felquer, F., Lonic, A., Bettess, M.D., Hamra, N., Semendric, L., Tan, B.S., Lake, J.A., Keough, R.A., et al. (2010). L-Proline induces differentiation of ES cells: a novel role for an amino acid in the regulation of pluripotent cells in culture. Am. J. Physiol. Cell Physiol. 298, C982–C992.

Ying, Q.L., Wray, J., Nichols, J., Batlle-Morera, L., Doble, B., Woodgett, J., Cohen, P., and Smith, A. (2008). The ground state of embryonic stem cell self-renewal. Nature 453, 519–523.